

## Crystal Engineering of Heterocyclic Arylene(ethynylene) Oligomers through Programmed Aromatic Stacking

William J. Mullin,<sup>a</sup> Peter Müller<sup>b</sup> Anthony J. Schaefer<sup>c</sup>, Elisa Guzman,<sup>a</sup> Steven E. Wheeler<sup>c</sup> and Samuel W. Thomas<sup>\*a</sup>

Received 00th January 20xx,  
Accepted 00th January 20xx

DOI: 10.1039/x0xx00000x

Conjugated oligomers and polymers consisting of aromatic heterocycles are examples of next-generation organic electronic materials. However, control and optimization of the self-assembly of these materials in the solid-state, which is a crucial parameter for high efficiency performance remains an unsolved challenge in materials development. In this work, we provide valuable insight into aromatic stacking interactions between fluorinated arene rings (ArF) and heterocycles different electronic character (Het), and elaborate on the prospect of using these interactions to control the solid-state configurations of three-ring phenylene-ethynylene oligomers (PEs). Oligomers possessing units typically thought of as electron-rich units (ER) show blue-shifted optical spectra in the solid-state, while those incorporating heterocycles typically thought of as electron deficient (ED) show red-shifted solid-state optical spectra. Crystal structures show ArF-Het stacking interactions between the fluorinated side-chains and ER units, which twist the PE backbone out of planarity and prevent chromophore aggregation. The interactions are absent in ED oligomers, highlighting the cofacial incompatibility between ArF rings and ED units. A combination of TD-DFT computations and novel heterocycle descriptors reinforce our assignment of the oligomers as ED and ER, while exhaustive conformer analysis shows ArF-Het stacking interactions are a significant contributor to compound stability. Overall, this work describes the importance of heterocycle electronics in conformational control in the solid state, understanding of which can be a valuable asset in the development of novel electronic materials.

### Introduction

Heteroaromatic ring systems that contain sulfur, oxygen, or nitrogen are present in nearly all modern conjugated polymers and oligomers, and have contributed to breakthroughs in the efficiencies of organic field-effect transistors<sup>1-4</sup>, photovoltaics<sup>5-8</sup>, and light emitting diode technology.<sup>9-11</sup> Combining electron donating and electron withdrawing heteroaromatic ring systems in conjugated materials enables precise control over HOMO and LUMO levels, redox potentials, and solution-state optical properties.<sup>12, 13</sup> Nevertheless, the inability to control or predict the solid-state molecular packing of conjugated materials continues to inhibit their widespread adoption.<sup>14</sup> The optical and electronic properties of conjugated solids depend critically on their packing, which in turn depends on competition between large numbers of weak non-covalent interactions (NCIs).<sup>15</sup> Heteroatoms can participate directly in specific NCIs, further exacerbating the challenge. Therefore, fundamental insight into the NCIs of heteroaromatics in the context of conjugated materials, and design strategies to control this

molecular packing, is important to improving their performance.

Specific NCIs of heterocycles can control intramolecular configuration and intermolecular coupling of conjugated materials. Most prevalent in this area are chalcogen interactions, which can improve backbone coplanarity of thiophene, selenophene, and benzothiadiazole containing units, increasing packing order and charge mobility in organic electronic devices.<sup>16-19</sup> Hydrogen bonds can also dictate the assembly of moieties common in conjugated materials, such as diketopyrrolopyrrole,<sup>20, 21</sup> naphthalene diimide,<sup>22, 23</sup> perylene diimide,<sup>24, 25</sup> and quinacridone.<sup>26, 27</sup> Hydrogen bonding side-chains pack tighter and yield self-healing properties, which benefits applications such as flexible transistors.<sup>28-30</sup> Finally, halogen bonding interactions involving heterocycle can dictate the luminescence properties of molecular cocrystals and supramolecular polymers.<sup>31-33</sup>

Because a large percentage of nearly all conjugated materials comprise aromatic rings, NCIs of arenes contribute strongly to the packing of such small molecules and polymers. Aromatic stacking interactions have also become important in drug design<sup>34</sup> and stimuli-responsive materials.<sup>35</sup> Extensive study and modeling of aromatic interactions<sup>36, 37</sup> have revealed a combination of electrostatic and dispersion contributions,<sup>38</sup> with arenes often forming edge-face interactions, which can yield herringbone packing motifs such as those found in pentacene.<sup>39, 40</sup> In contrast, the perfluoroarene-arene (ArF-ArH) cofacial stacking is a powerful supramolecular synthon across

<sup>a</sup> Department of Chemistry, Tufts University, 62 Talbot Ave, Medford, MA 02155, USA. Email: sam.thomas@tufts.edu

<sup>b</sup> Department of Chemistry, Massachusetts Institute of Technology, Cambridge, MA 02139, USA.

<sup>c</sup> Department of Chemistry, University of Georgia, Athens, GA 30602, USA.

Electronic Supplementary Information (ESI) available: Full experimental section, NMR and optical spectra, descriptions of crystallography, including descriptions of conformations searches and TD-DFT computations. See DOI: 10.1039/x0xx00000x

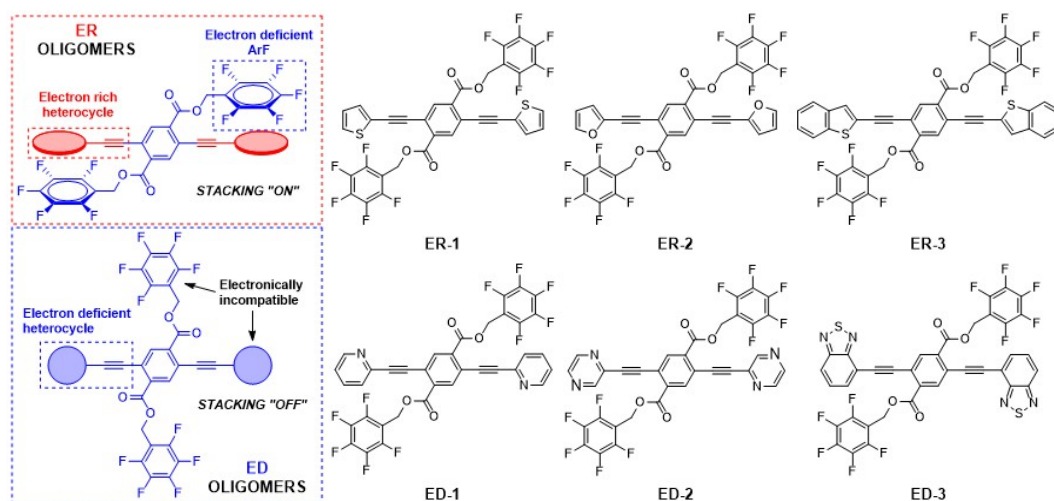
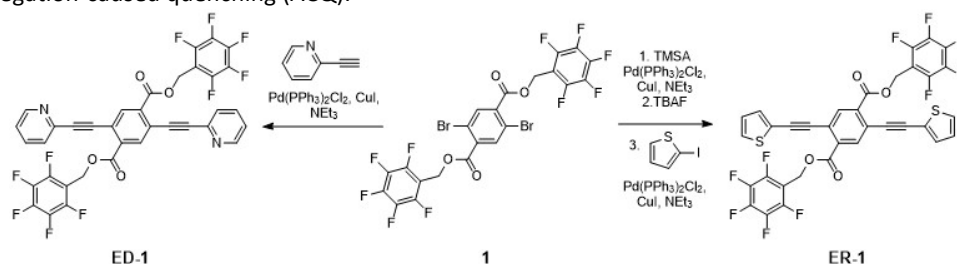


**Figure 1.** Left: Schematic representation of new ER and ED oligomers demonstrating the dependence of heterocyclic electronic character on stacking ability. Right: Chemical structures of fluorinated ER and ED oligomers presented in this work.

materials science and chemical biology.<sup>41, 42</sup> Although fundamental understanding of aromatic interactions of benzene and substituted phenylene derivatives are well developed, relying on electrostatic complementarity as a key parameter, extension of these models to heteroaromatic systems is infrequent. Reported examples of intermolecular stacking interactions between perfluoroarenes and heteroarenes include thiophene,<sup>43, 44</sup> furan<sup>45-47</sup>, and imidazole,<sup>48</sup> while stacking appears less likely between electron deficient units such as pyridine.<sup>49-52</sup> Combining the power of the ArF-ArH cofacial interaction in designing solid-state packing with the prevalence of various heteroarenes in the highest-performance conjugated materials reveals the importance of understanding how heteroarene structure influences ArF-ArH interactions.

Poly- and oligo(arylene-ethynylenes) (AEs) are a class of conjugated materials with alternating aromatic units and carbon-carbon-triple bonds.<sup>53</sup> Their optoelectronic properties are largely dictated by their chemical structure, and incorporating different heterocycles into the conjugated backbone can help tune their optical bandgaps.<sup>54</sup> As a consequence of the low barrier of rotation about the triple-bond, wide ranges of conformers are accessible, making it difficult to control and dictate the intra- and intermolecular packing in the solid-state.<sup>55</sup> This is problematic from a materials design perspective, as the solid-state optical properties are heavily influenced by this packing, often resulting in shifting of emission and aggregation-caused quenching (ACQ).<sup>56-58</sup>

Our group has demonstrated that programmed aromatic stacking interactions between non-conjugated fluorinated ester side-chains and main-chain arene groups can control solid-state packing of phenylene-ethynylenes PEs.<sup>59-63</sup> In agreement with prior work showing that the electrostatic complementarity of arene rings plays a pivotal role in determining the likelihood of aromatic stacking,<sup>64, 65</sup> our 2017 study on electronic substituent effects for ArF-ArH stacking demonstrated the need for electronic complementarity between stacking partners. The electron deficiency of the ArF ring required a sufficiently electron rich partner for cofacial ArF-ArH stacking to occur. To accommodate this intramolecular stacking interaction in our PE structures, the chromophore twists out of planarity by 55-85°, while intermolecular ArF-ArH interactions prevent aggregation between the PE chromophores, which combined have strong effects on their solid-state electronic spectroscopy, including imparting mechanofluorochromism. Given their importance to organic optoelectronics, we here extend our experimental approach to perfluoroarene stacking with heteroaromatics, the electronic characteristics of which cannot be simply parametrized by Hammett substituent constants. Understanding how heterocycle structure influences observed NCIs, overall packing motifs, and optical properties yields valuable insight into stacking between fluorinated arene rings and heterocycles, further establishing this supramolecular synthon as an effective handle to exert control over the solid-state packing of conjugated materials.



**Scheme 1.** Examples of coupling reactions used to prepare fluorinated and non-fluorinated PE oligomers.

## Results and Discussion

As aromatic heterocycles also possess inherent electronic character, we expected that molecules possessing more electron-rich heterocycles would be more likely to demonstrate stacking and twisting than molecules containing electron-deficient heterocycles (**Figure 1**). To test this hypothesis, we prepared six pairs of arylene-ethynylene (AE) oligomers, each comprising a benzyl ester substituted terephthalate core bound to monocyclic or bicyclic heteroarenes through triple bonds. Two classes of oligomers have been developed: **ER oligomers** with “electron-rich” heterocycles and **ED oligomers** with “electron-deficient” heterocycles. We classify these molecules according to the electronic classification of the heterocycles: **ER-1**, **ER-2**, and **ER-3** possess heterocycles generally considered more “electron rich” (thiophene, furan, and benzothiophene), while **ED 1**, **ED-2**, and **ED-3** possess heterocycles generally considered more “electron deficient” (pyridine, pyrazine, and benzothiadiazole). To understand the influence of the ArF pendants on optical properties and solid-state assembly, we also compared each fluorinated compound to its analog containing unsubstituted benzyl ester groups, denoted with an **H** in their name (e.g. **ER-1H**). The synthesis of these compounds begins with esterification of commercially available 2,5-dibromoterephthalic acid with either benzyl or perfluorobenzyl alcohol. Two similar pathways yielded the target compounds (**Scheme 1**): i) ethynylation of the dibenzylterephthalate, followed by Sonogashira coupling with the monohalogenated heterocycle, or 2) ethynylation of the heterocycle followed by Sonogashira coupling to the dibenzylterephthalate core—Pages S1-S11 of the Electronic Supplementary Information contains the details of the syntheses of all compounds described herein.

### Electronic Optical Spectroscopy

As summarized in **Figure 2**, the trends of absorbance and emission spectra for these compounds in chloroform correlate with the electronic characteristics of the conjugated heterocycles, consistent with donor-acceptor-donor of the ER compounds, and an all-acceptor character of the ED derivatives. Those with more electron rich monocyclic heteroaromatic thiophene (**ER-1**) and furan (**ER-2**) have red shifted emission and absorbance spectra compared to **ED-1** and **ED-2**, which contain more electron deficient pyridine and pyrazine rings. The fused bicyclic derivatives also follow this trend, with red shifts in the absorbance (11 nm) and emission (28 nm) spectra of benzothiophene-containing **ER-3** compared to benzothiadiazole-containing **ED-3**. In addition, the three ER oligomers all demonstrate positive solvatochromism, while the optical spectra of the ED oligomers do not change in response to solvent polarity—emission spectra of the **ER** oligomers in acetonitrile were red-shifted 20–35 nm compared to the same molecules in toluene, while **ED** oligomers showed no change in different solvents (See **Figure S23–Figures S38** in the Electronic Supplementary Information for all spectra).

To assess the impact of pendant fluorination on solution state optical properties, we compared optical spectra of the fluorinated oligomers and their non-fluorinated control

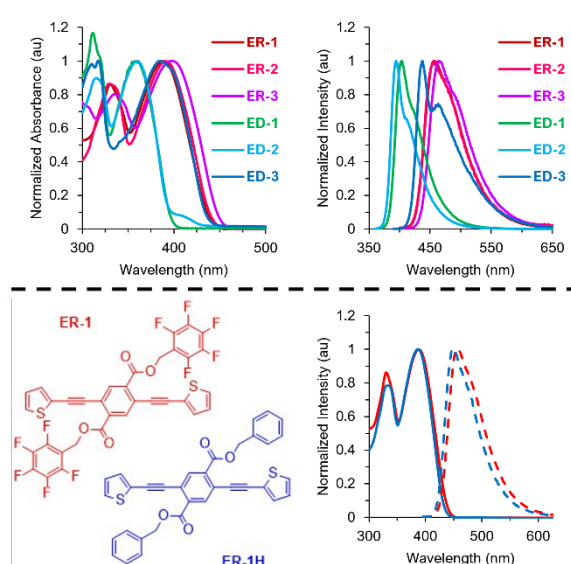


**Figure 2.** Top left: absorbance spectra of fluorinated ED and ER oligomers in dilute chloroform solution. Top right: emission spectra of fluorinated ED and ER oligomers in dilute chloroform solution. Bottom left: chemical structures of fluorinated **ER-1** and non-fluorinated control analogue **ER-1H**. Bottom right: Absorbance (solid lines) and emission (dashed lines) of **ER-1** (red) and **ER-1H** (blue) in dilute chloroform solution.

analog, an example of which is provided in **Figure 2**. In dilute solution, the spectral positioning of emission and absorbance, as well as quantum yield, of **ER-1** and **ER-1H** were nearly indistinguishable: the spectral maxima for each fluorinated and non-fluorinated pair are within 5 nm of each other. We attribute the modest differences to inductive effects of the fluorinated side-chains increasing the electron-withdrawing character of the terephthalate unit. These data suggest that in solution, the electronics of the PE chromophore itself dictate the electronic structure of each molecule, which the non-conjugated side chains do not influence. This result agrees with the typical design paradigm regarding electronic insulation of side chains from the  $\pi$ -conjugated chromophore.

The solid-state optical properties of PEs depend strongly on intramolecular conformations and intermolecular aggregation, as the low barrier to rotation of PEs allows for a wide range of conformations of their backbones. To understand how the structure of the heteroarenes impact optical properties as solids, we compared the spectra of thin films that were drop-cast onto glass slides, followed annealing at 100°C to mitigate residual solvent effects. Their solid-state optical behavior depends strongly on whether the heteroaromatic ring in the PE backbone is in the “ER” or “ED” group. **Figure 3** shows optical spectra of ER thin films compared to those in dilute solution. Relative to their absorbance spectra in dilute chloroform solution, the excitation spectra of **ER-1** and **ER-3** films show hypsochromic shifts of the lowest energy transition of 29 nm and 34 nm, respectively. **ER-2** shows a small 25 nm bathochromic shift in the onset of excitation, while the maximum of the lowest energy transition remains nearly identical. Fluorescence emission spectra of the ER compounds showed similarly small differences between solution and solid-state spectra: emission spectra of solid **ER-1** and **ER-3** are blue shifted by 11 nm and 5 nm, respectively, while **ER-2** shows

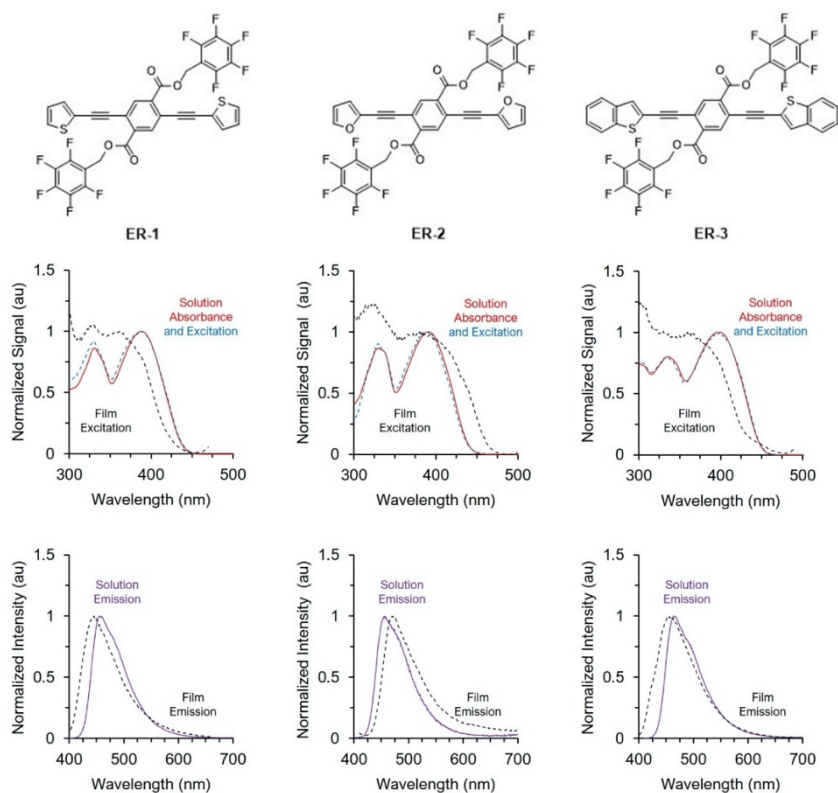


**Figure 3.** Optical spectra of **ER-1**, **ER-2**, and **ER-3** in dilute chloroform solution and as drop-cast films. All thin films were heated to 100 °C for 10 min after solvent evaporated at ambient temperature.

bathochromic shifting of 15 nm. In contrast, all three ED molecules display bathochromic shifts in their excitation and emission spectra (Figure 4). The ranges of excitation onset and emission maxima shift are 35–55 nm and 36–106 nm, respectively, all of which are larger than the ER molecules.

To better understand the impact of ArF side-chains on solid-state optical properties, emission and excitation spectra of each control oligomer were compared to their fluorinated analogues. All six non-fluorinated oligomers, regardless of the conjugated heterocycle, demonstrated large bathochromic shifts of solid-state spectra in both excitation and emission maxima when compared to the same compound in dilute chloroform solution. **Figure 5** shows an example of this for **ER-3** and **ER-3H**; the Electronic Supplementary Information contains comparisons of spectra for all pairs of analogs. Relative to fluorinated **ER-3**, **ER-3H** shows large bathochromic shifts of 40 nm and 72 nm in excitation onset and emission maximum, respectively. Altogether, these results suggest that interactions of ArF rings with electron rich heterocycles can prevent PE planarization and interchromophore aggregation.

The dynamic nature of the ethynyl linkages and the weak nature of non-covalent interactions can imbue these molecules with mechanofluorochromic (MFC) behavior (**Figure 6**). The emission spectra of compounds **ER-1** (52 nm) **ER-2** (47 nm) and **ER-3** (67 nm) shifted to the red notably upon grinding, which we attribute to force-induced planarization and aggregation of the chromophore backbones. Heating these ground films to a temperature 10–20° below their melting points causes at least partial recovery of the original emission. In contrast, grinding

films of **ED-2** and **ED-3** yield hypsochromic shifts of 17 nm and 44 nm, respectively, while **ED-1** films produce only negligible change. We attribute this hypsochromic shifting to the shear force disrupting J-type aggregates in the ED compounds—packing of these molecules are consistent with J-aggregation (vide infra). The slip angle of **ED-3** was measured to be 47°. Finally, none of the non-fluorinated control compounds exhibited observable MFC at room temperature, further highlighting that the pendant ArF rings play a critical role in dictating the solid-state optical properties of these oligomers. (See **Figure S35–Figures S37** in the Electronic Supplementary Information for all MFC spectra).

In summary, several trends of the optical properties of these compounds emerge. First, ER derivatives possess red-shifted absorbance and emission spectra in solution compared to the ED oligomers, owing to their donor-acceptor-donor structure, which is further supported by the presence of positive solvatochromism. Second, ER oligomers demonstrate slightly blue-shifted or slightly red-shifted emission and excitation spectra upon transition to the solid-state, while ED oligomer thin films show large bathochromic shifts from solution. We further note that the trends in solid-state optical data of the ED oligomers resemble that of all six of the non-fluorinated control oligomers. Third, the emission spectra of ER oligomers shift bathochromically when ground, while ED oligomers tend to shift hypsochromically. These trends suggest significant

differences in the packing patterns between ER, ED, and control oligomers.

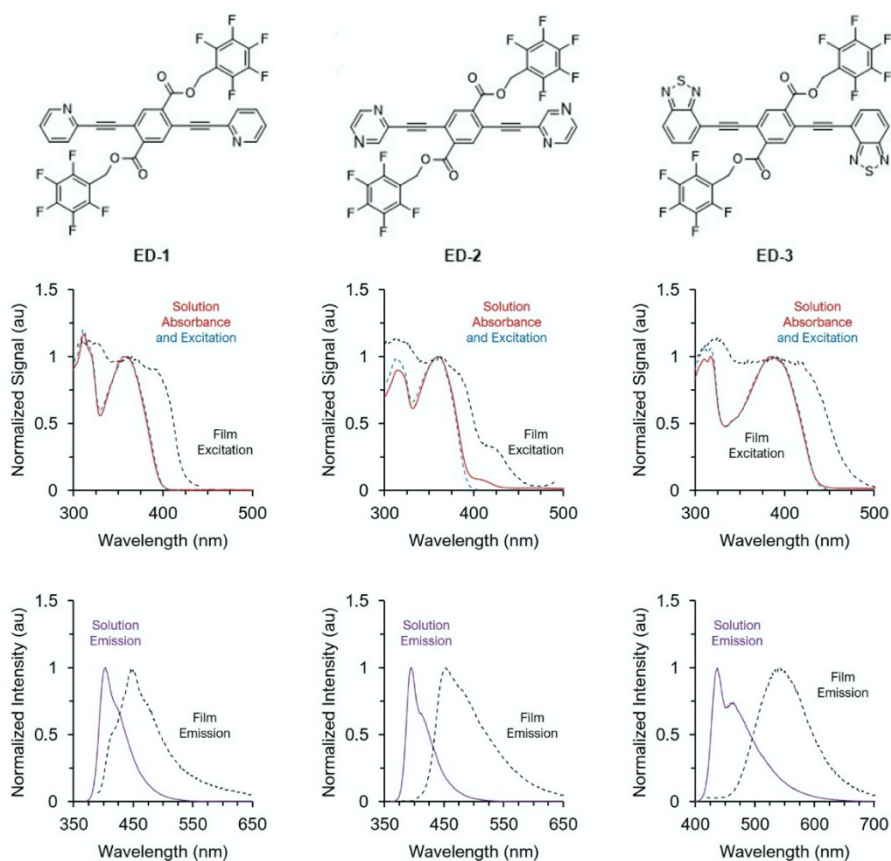


**Figure 4.** Optical spectra of **ED-1**, **ED-2**, and **ED-3** in dilute chloroform solution and as drop-cast films. All thin films were heated to 100 °C for 10 min after solvent evaporated at ambient temperature.

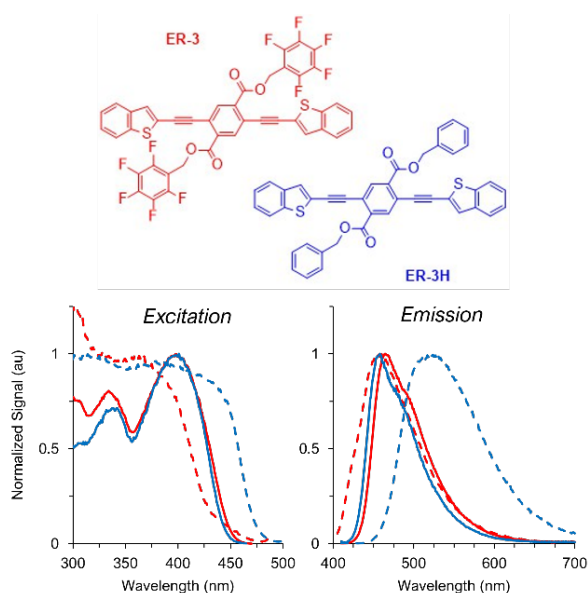


**Figure 5.** Excitation (left) and emission (right) spectra of **ER-3** (red) and **ER-3H** (blue) in solution (solid line) and thin film (dashed line). All thin films were heated to 100 °C for 10 min after solvent evaporated at ambient temperature.

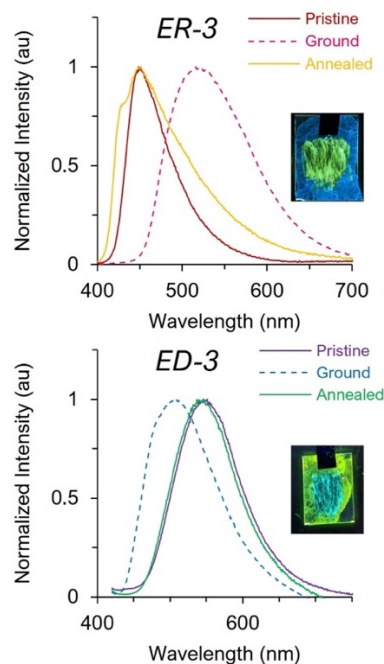


**Figure 6.** Exemplar mechanofluorochromic responses of **ER-3** and **ED-3**. All films were drop cast from chloroform, ground with a metal spatula, and annealed to within 20 °C of their melting points. Insets show photographs of ground thin film samples under illumination with a handheld UV lamp.

## X-ray Crystallography

We have determined the single crystal X-ray structures eight of the twelve compounds in this paper. Crystals were either grown from slow evaporation or diffusion of hexanes into chloroform solutions (See Page S48 of the ESI for details). For the fluorinated oligomers, we acquired structures of **ER-1**, **ER-3**, **ED-1** and **ED-3**. The differences in packing between these structures demonstrate how both the ArF side chains and heterocycles in the PE backbone determine conformation and intermolecular configuration. In addition, X-ray crystal structures of non-fluorinated compounds **ER-1H**, **ER-2H**, **ED-2H** and **ED-3H** serve as comparative references in two ways: i) further elaborating on the significance of the ArF side-chains and ii) as a basis for inferring the packing patterns of fluorinated structures we have not been able to determine.

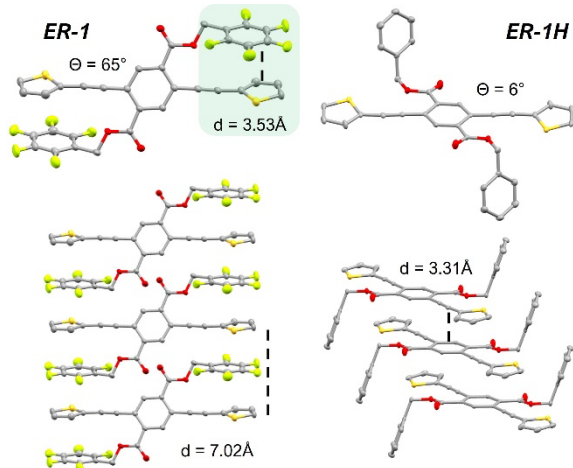


**Figure 7.** Single crystal X-ray structures of **ER-1** and **ER-1H**. An ArF-Het interaction is highlighted by a green box.  $\Theta$  indicates torsional angles along the conjugated backbones;  $d$  refers to distances between rings/chromophores. Thermal ellipsoids are shown at 50% probability, and hydrogen atoms have been removed for clarity.

**Figure 7** shows a comparison of the X-ray crystal structure of the two thiophene-containing analogs, **ER-1** and **ER-1H**. **ER-1** features intramolecular cofacial stacking interactions between the thiophene rings and the ArF side-chains with 3.5–3.6 Å inter-ring spacing. To accommodate these intramolecular cofacial interactions, the arylene-ethynylene backbone twists out of conjugation with torsional angles of  $\sim 65^\circ$ . The ArF and thiophene rings of **ER-1** also stack intermolecularly, which shields the chromophore main chains from aggregation. In contrast, the backbone of **ER-1H** is nearly planar (torsional angle  $\sim 3^\circ$ ), allowing for close chromophore aggregation, with separation distances between the chromophores of 3.3 Å. The pitch and roll distance between cofacially stacked chromophores are 3.7 Å and 0.1 Å, respectively, forming a herringbone-type pattern. The unsubstituted benzyl pendants form slipped stacks with those of neighboring molecules, with interplanar distances of 3.4 Å. This combination of planarization and aggregation red-shifts the solid-state excitation and emission of **ER-1H** from those of the twisted and shielded **ER-1** by 35 nm and 43 nm, respectively.

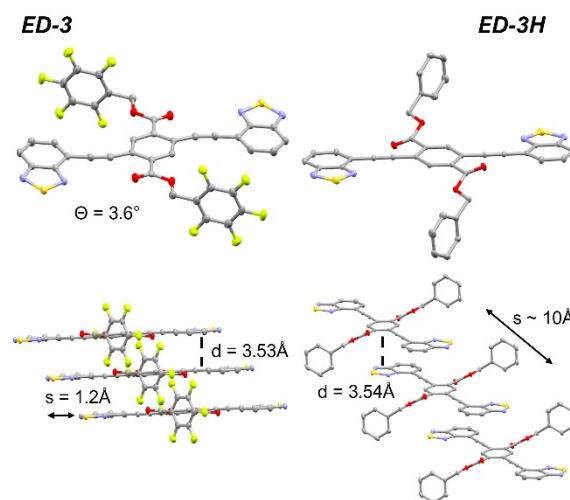


**Figure 8.** Crystal packing diagrams of **ED-3** and **ED-3H**.  $\Theta$  indicates torsional angles along the conjugated backbone,  $s$  refers to slip distances between chromophores, and  $d$  refers to distances between rings/chromophores. Thermal ellipsoids shown at 50% probability, and hydrogen atoms have been removed for clarity.

In contrast to **ER-1** and **ER-1H**, the packing patterns of **ED-3** and **ED-3H** show distinct similarities to each other, even with the differing substitution of their pendant benzyl esters (**Figure 8**). The conjugated backbones of both compounds show torsional angles smaller than  $6^\circ$ . In addition, the PE chromophores of both structures aggregate with separation distances of approximately 3.3 Å. The most striking difference between the packing patterns lies in the slip distances parallel to the long axis of the PE backbones between the cofacially aggregated chromophores. The slip distance between chromophores of **ED-3H** exceeds 10 Å, while the slip distances between adjacent **ED-3** chromophores is approximately 1.2 Å. We attribute this result to differing interactions of either the fluorinated or protonated side-chains. The ArF pendants in **ED-3** interact in a slip-stacked sandwich-like dimer, stabilized by the alignment of the local C—F bond dipoles, keeping the chromophores closer together along their long axes. On the other hand, the ArH pendants in **ED-3H** do not interact intramolecularly with their respective chromophores. Instead, they interact intermolecularly with neighboring molecules as highly slipped dimers. In addition, the sulfur atom of a neighboring benziothiadiaazole group is located 3.3 Å above the ArH ring.

Additional crystal structures of both **ED** and **ER** fluorinated oligomers further highlight the how electronic complementarity correlates with stacking interactions in the solid state. **Figure 9** shows the packing of **ER-3**, which contains electron rich benzothiophenes, and **ED-1**, which contains electron withdrawing pyridines. The structure of **ER-3** resembles **ER-1** as ArF-ArH stacking interactions twist the conjugated backbone out of planarity and prevent chromophore aggregation, with torsional angles and interchromophore distances of  $58^\circ$  and 6.8 Å, respectively.

Table 1. Excitation, emission and mechanofluorochromic parameters of fluorinated ER and ED oligomers in CHCl<sub>3</sub> and drop-cast thin films.

Compound	Excitation			Emission			Mechanofluorochromism				
	Solution	Film	Shift	Solution	Film	Shift	$\Phi_f^a$	$\tau$ (ns) <sup>a</sup>	Pristine	Ground	Shift
ER-1	386	365	-21	456	445	-11	0.18	0.7	438	490	52
ER-2	391	380	-11	456	470	14	0.24	2.6	467	514	47
ER-3	398	365	-33	465	460	-5	0.48	1.1	449	516	67
ED-1	360	389	29	404	436	32	0.47	-	436	446	10
ED-2	360	363	3	394	453	59	0.42	-	461	444	-17
ED-3	387	415	28	437	543	106	0.86	1.4	551	507	-44

<sup>a</sup> Quantum yields and lifetimes reported in dilute chloroform solutions.

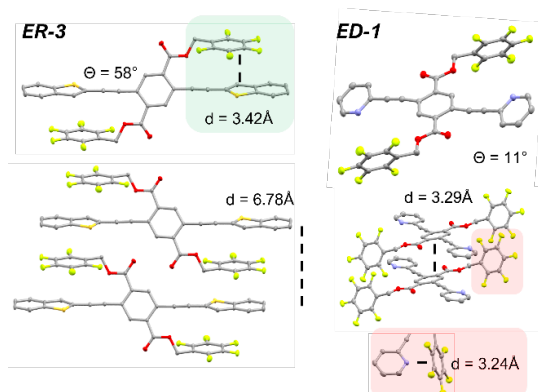


**Figure 9.** Crystal packing diagrams of ER-3 and ED-1. Thermal ellipsoids are shown at 50% probability, and hydrogen atoms have been removed for clarity.

ED-1 packs similarly to ED-3, with planar, aggregated chromophores. A notable feature of the ED-1 crystal structure is the interaction between the nitrogen atoms in the pyridine rings and the faces of ArF rings of neighboring molecules, with the two rings arranged perpendicular. Consistent with the hypothesis that this interaction is an important stabilizing force for this specific crystal lattice, our computation reveals that this interaction provides more than 5 kcal/mol of stabilization, which suggests a favorable interaction between the nitrogen lone-pair and the face of the ArF ring, termed an N- $\pi^*$  interaction.<sup>66</sup> SAPT0/jun-cc-pVDZ<sup>67-71</sup> analysis of this interaction reveals that it is primarily driven by dispersion interactions (-4.1 kcal/mol) but also has a strong electrostatic component (-2.7 kcal/mol).

Finally, we have elucidated the structures for two additional non-fluorinated compounds, ER-2H and ED-2H. These planar and aggregated chromophores resemble the ED and other non-fluorinated oligomers. While these structures do not give explicit information about their fluorinated counterparts, we infer, based on solid-state optical data and their crystal structures, that ER-2 packs similarly to ER-1 or ER-3, and ED-1 packs similarly to ER-2H respectively (See Figures S39 and S40 in the Electronic Supplementary Information for structures). This set of observations is particularly important for ER-2, as this

compound demonstrates slight bathochromic shifting in its solid-state emission spectrum in contrast to the hypsochromic shifting exhibited by ER-1 and ER-3. Emission shifting in ER-2H is approximately 80 nm compared to the 14 nm shift of ER-2. Based on this disparity, we believe that the propensity of backbone planarity and aggregation in ER-2 is lower than ER-2H. In addition, we have published additional examples of 3-ring PE compounds with twisted backbones whose emission spectra are slightly shifted bathochromically from solution.<sup>59</sup>

To summarize, single crystal X-ray structures provide insight into how ArF-ArH interactions depend on chemical structure and correlate with solid-state optical data. ER-1 and ER-3 exhibit twisted and separated chromophore backbones as a result as of ArF-ArH stacking interactions. This twisting motif interrupts conjugation along their backbones, shortening the length of conjugation, preventing aggregation, and thereby increasing bandgap. When the same chromophores are appended with hydrogenated pendants, as in the case of ER-1H, backbone planarity and aggregation is unencumbered, shrinking the bandgaps of these solids. Despite the presence of ArF rings in their side-chains, similar red-shifting is observed in ED-1 and ED-3, whose conjugated backbones are nearly planar and aggregated, resembling ED-3H. We therefore conclude that the ArF-ArH stacking interactions dictate the optical properties of these solids and that the electronic characteristics of the potential heterocyclic stacking partner play a major role in determining whether these interactions occur.

### Computational Search for Low-Energy Conformations

An exhaustive computational search of low-lying conformations of these compounds at the PCM- $\omega$ B97X-D/def2TZVP// $\omega$ B97X-D/def2SVP level of theory<sup>72,73</sup> was conducted to understand the conformational behavior of the isolated oligomers in chloroform. Consistent with the shallow potential energy surface known for arylene ethynyls, this process revealed dozens of unique thermodynamically accessible conformations for each compound (see Table 2). The non-fluorinated analogs, in general, exhibited significantly more low-lying conformations. For example, whereas for ER-1 there are 15 unique conformers within 3 kcal/mol of the global minimum

structure, for **ER-1H** there are 42, and are therefore predicted to be present in significant populations in solution. Remarkably, across all twelve structures, between four and eleven of these conformations lie below 1 kcal/mol.

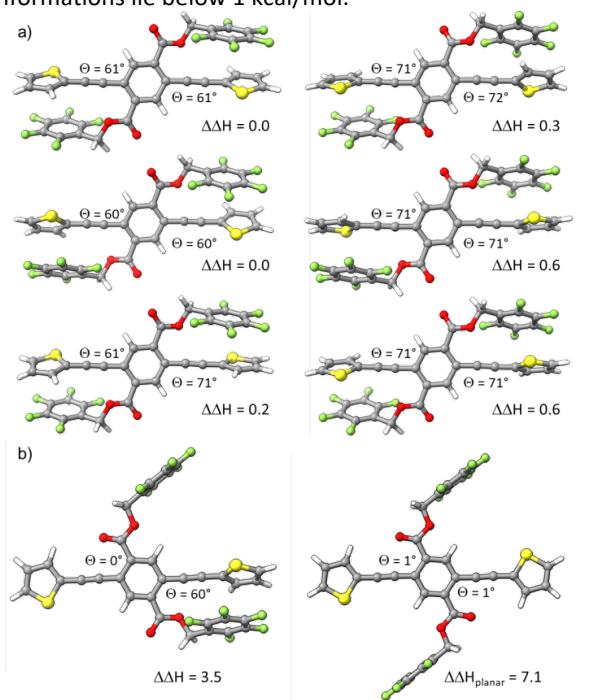


**Figure 10:** a) Solution-phase conformers of **ER-1** within 1 kcal/mol of the global minimum structure; b) selected conformations with partially or fully planar backbones.  $\Theta$  indicates torsional angles along the conjugated backbone;  $\Delta\Delta H$  is the relative enthalpy at 298K in kcal/mol.

The six lowest-lying conformations of **ER-1** are shown in **Figure 10a**, along with the relative enthalpies and backbone torsion angles. These structures are representative of the low-lying conformations of all of the oligomers. Each of these conformations exhibits some degree of intramolecular stacking interactions, resulting in fully twisted backbones. Other selected conformations of **ER-1** are shown in **Figure 10b**. The lowest-lying structure with a half-planar backbone lies 3.5 kcal/mol higher in enthalpy than the global minimum, while the relative enthalpy of the fully planar conformation is 7.1 kcal/mol. Thus, in solution both the **ED** and **ER** oligomers are highly conformationally dynamic but strongly favor closed conformations with twisted backbones.

The relative enthalpies of the fully planar conformations ( $\Delta\Delta H_{\text{planar}}$ ) are listed in Table 2 for all of the oligomers and are similar for both the **ER** and **ED** oligomers. If anything, the **ER** oligomers exhibit slightly smaller enthalpy differences than the similarly sized electron-poor oligomers, in apparent contrast with the overall design principle described above in which electron-rich heterocycles engage in more favorable intramolecular stacking interactions with the perfluorophenyl ring, compared to electron-poor heterocycles. This finding highlights the importance of dispersion forces in determining overall interaction strengths, in addition to electrostatic effects. That the two bicyclic heterocycles—benzothiophene and benzothiadiazole—yield the largest  $\Delta\Delta H$  further reinforces this

interpretation. Indeed, SAPT0/jun-cc-pVDZ analyses on the stacked thiophene-perfluorophenyl and benzothiophene-perfluorophenyl dimers in the lowest-lying conformations of **ER-1** and **ER-3**, respectively, reveal that the latter benefits from 2.4 kcal/mol of additional stabilizing dispersion interactions (-9.2 vs -11.6 kcal/mol). Moreover, this finding indicates that in the case of the **ER** oligomers, intermolecular interactions in the solid state are insufficient to overcome the preference of these systems to engage in intramolecular stacking interactions, while the opposite occurs for the **ED** oligomers. Thus, it seems that the tuning provided by varying the flanking heterocycles impacts the competition between intermolecular non-covalent interactions at least as much as it does the intramolecular stacking interactions. Finally, the enthalpy required to achieve a planar backbone is systematically much smaller for the hydrogenated oligomers, explaining why none of the hydrogenated oligomers exhibit the twisted conformation in the solid state—the relatively small difference in enthalpy favoring intramolecular stacking interactions is easily overshadowed by alternative intermolecular contacts in the solid state.

Table 2. Summary of solution-phase conformers.

	Number of Conformers		$\Delta\Delta H_{\text{planar}}$ (kcal/mol)
	$\Delta\Delta H < 3$ kcal/mol	$\Delta\Delta H < 1$ kcal/mol	
<b>ER-1</b>	15	6	7.1
<b>ER-2</b>	24	6	5.7
<b>ER-3</b>	14	6	9.1
<b>ED-1</b>	15	6	7.9
<b>ED-2</b>	17	5	6.7
<b>ED-3</b>	10	6	10.6
<b>ER-1H</b>	42	10	5.3
<b>ER-2H</b>	34	4	5.2
<b>ER-3H</b>	28	5	6.7
<b>ED-1H</b>	29	5	6.3
<b>ED-2H</b>	27	11	6.5
<b>ED-3H</b>	14	4	8.6

To further understand the impact of conformations on the excitation spectra of these oligomers, we employed TD-DFT computations at the PCM-PBE0/def2TZP level of theory (chloroform as solvent)<sup>73-75</sup> using the gas-phase  $\omega$ B97X-D/def2SVP optimized geometries. Solution-phase UV-vis absorption spectra based on a Boltzmann weighting of all low-lying conformations are depicted in **Figure 11**. While the absorption peaks are shifted slightly relative to the experimental solution-phase spectra (e.g. Table 1), they can still provide insight into the observed photophysical behavior. Also shown are predicted spectra for the single conformation observed (or presumed) in the solid state. In the case of the **ER** oligomers, there are relatively small shifts in  $\lambda_{\text{max}}$  since the conformations in the solid state match the low-lying solution-phase structures. Effects of the solid-state environment likely contribute to the experimentally observed blue shifts. The **ED** oligomers, on the other hand, exhibit a consistent shift of ~50 nm due to the planarization of the conjugated backbone going

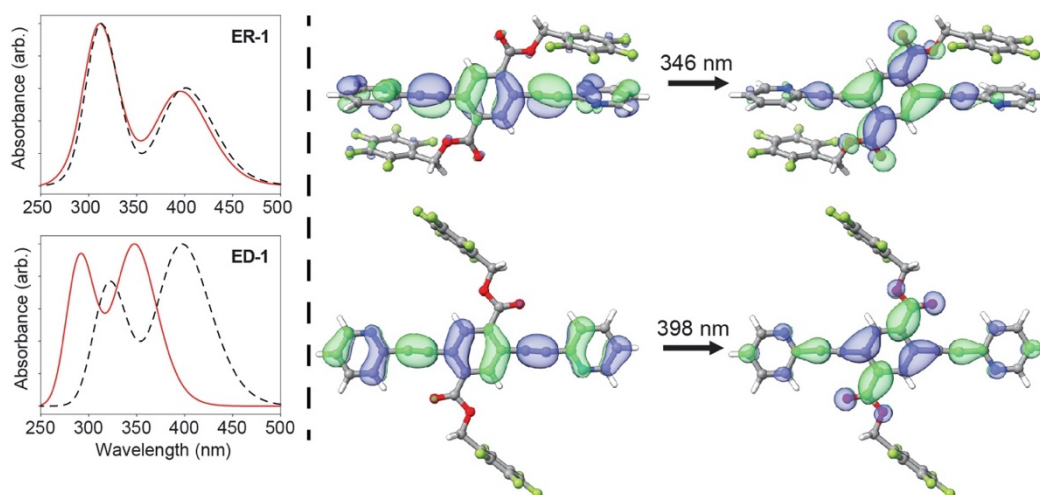


**Figure 11.** Left: TD-DFT UV-vis absorption spectra. Boltzmann-weighted spectra in chloroform in red; gas-phase spectrum of the (presumed) solid state conformation in black (twisted conformation for the ER oligomers, fully planar conformation for the ED oligomers). Right: NTOs for the lowest-energy transition for the twisted (top) and planar (bottom) conformations of ED-1.

from the solution-phase conformations to the solid state. Natural transition orbitals (NTOs) for the lowest-energy excitation in the twisted and planar conformations of ED-1 are shown in Figure 11. In both cases the transition is between an orbital that is delocalized across the conjugated backbone to one more localized on the terephthalate core. In the case of the planar conformation observed in the solid state for ED-1, this orbital is more delocalized into the pyridyl rings, explaining the observed red shift in  $\lambda_{\max}$ .

### Correlation of Experimental Results with Electrostatic Potential Descriptors for Heterocycles

While the concepts of electron poor and electron rich heterocycles are clear in a qualitative sense and form the basis of the design of conjugated materials such as donor-acceptor polymers, attempts to quantify these characteristics are rife with complications and there is no clear quantitative measure of electron deficiency. The wide diversity of heteroarene structure poses a challenge to establishing a unified approach to this quantification, in contrast to substituted phenylenes for which Hammett substituent coefficients are commonly used. We note that as described above, solvatochromism studies support our conclusion that the heterocycles in the ER compounds have donor character while the heterocycles of the ED compounds do not. In an approach tailored towards predicting and rationalizing the relative strengths of aromatic stacking interactions, Bootsma and Wheeler<sup>37</sup> introduced several heterocycle descriptors based on computed electrostatic potentials (ESPs) that provide a proxy for electron deficient character while also capturing key aspects of stacking interactions in drug-design contexts.<sup>36, 76, 77</sup> Among these descriptors, we have found in this study that the mean value of the ESP in the projection of the van der Waals volume of the heterocycle onto a plane 3.25 Å from the heterocycle ( $ESP_{\text{mean}}$ ) provides a clear differentiation between the pendant aryl groups in the ER ( $ESP_{\text{mean}} = -4.9$  to  $-3.9$ ) and ED ( $ESP_{\text{mean}} = -2.7$  to  $-0.9$ ) oligomers examined here. Moreover, this descriptor

correlates with both crystallographic (see Figure 12) and spectroscopic (see Figure 13) observations. The correlation of this parameter, which directly probes electrostatic potential at a distance typical for cofacial stacking, with these experimental trends provides theoretical support for our model of electrostatic complementarity between the ArF perfluorinated rings and the ArH heterocycles playing a determinative role in the solid-state assembly and properties of these conjugated materials.

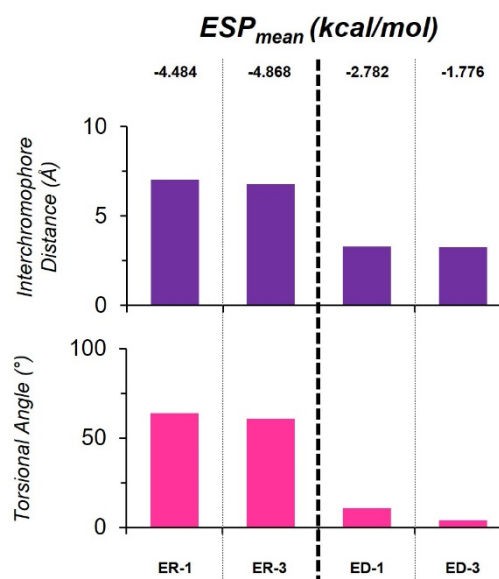


**Figure 12:** Summary of the correlations between mean ESP values for heterocycles and crystallographic parameters.

### Conclusions

In this work, we presented 12 new PE compounds that provide valuable insight into the stacking interactions between fluorinated aromatic rings and heterocycles of varying electronic character. Optical spectra of these compounds in solution and the solid state suggest that the presence of

stacking interactions can have a profound effect on the changes of emitted light upon transitioning to a thin film state, as well as control over the mechanism and magnitude of stimuli-responsive behavior such as MFC. Crystallographic data suggest that the electronic relationship between the side-chains and main-chain heterocyclic fragments plays a critical role in whether or not stacking will occur in the solid state. Pairing the electron deficient ArF ring with more traditionally electron-rich heterocycles increases the likelihood of ArF-ArH stacking observed in the crystal structures. Electron deficient units highlight the need for electronic complementarity between stacking partners.

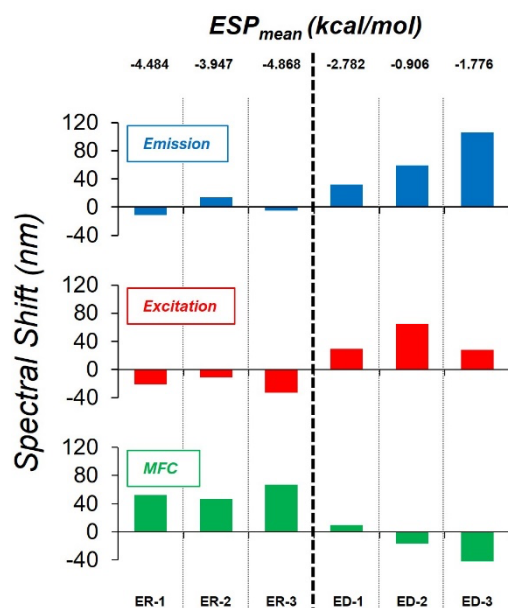


**Figure 13:** Summary of the correlations between the mean ESP values and spectroscopic observations, including emission, excitation, and mechanofluorochromism shift.

Computational methods corroborate these interpretations of experimental trends. In solution, these arylene ethynyls with both electron-rich and electron-poor heterocycles exist as an ensemble of conformations with twisted backbones. In the solid state, intermolecular interactions are sufficient to overwhelm the inherent preference for intramolecular stacking in the case of the electron-deficient systems, yielding conformations with planar backbones and strongly red-shifted optical spectra. In the case of the electron-rich heterocycles, the intramolecular and intermolecular ArF-ArH stacking interactions are sufficiently strong that they persist in the solid state, but lock the individual oligomers into conformations that are slightly blue shifted relative to the solution-phase ensemble.

Given the near universal inclusion of increasingly complex heteroaromatic ring systems in cutting-edge conjugated materials, such robust and alternative design approaches are critical for optimization and materials discovery. Although our computational work suggests that varying the nature of these heterocycles tunes a delicate balance between a range of intermolecular interactions in the solid state, the readily calculated mean ESP value provides a potentially useful

parameter, beyond the traditional Hammett coefficients, for predicting the propensity of cofacial stacking of a diverse collection of ring systems. Developing an experimentally supported library of these mean ESP values would provide valuable insight into the packing patterns of conjugated materials that incorporate heterocycles, which would be beneficial for the fields of organic electronics and drug design. Efforts are currently ongoing to construct such a library, and molecules will be prepared to provide a measure of validation. This successful merger of thorough experimental results with computational approaches grounded in mechanisms of interaction both rationalizes the observed trends of compounds described in this individual study, and points towards possible paths forward for rational design of discrete non-covalent aromatic interactions within conjugated materials.

## Conflicts of interest

There are no conflicts of interest to declare.

## Acknowledgements

This work was supported by the U.S. Department of Energy, Basic Energy Sciences, through award DE-SC0016423. E.G. was supported by an NSF Graduate Research Fellowship. The molecular structures in Figures 10 and 11 were made using ChimeraX<sup>78</sup> with the SEQCROW plugin,<sup>79</sup> while the simulated UV-vis spectra were generated using AaronTools.<sup>80</sup> All computations were done using Gaussian 16.

## Notes and references

1. S. Bi, Y. Li, Z. He, Z. Ouyang, Q. Guo and C. Jiang, *Org. Electron.*, 2019, **65**, 96-99.
2. Y. Q. Zheng, T. Lei, J. H. Dou, X. Xia, J. Y. Wang, C. J. Liu and J. Pei, *Adv. Mater.*, 2016, **28**, 7213-7219.
3. B. Sun, W. Hong, Z. Yan, H. Aziz and Y. Li, *Adv. Mater.*, 2014, **26**, 2636-2642.
4. J. Wang and X. Zhan, *Acc. Chem. Res.*, 2021, **54**, 132-143.
5. T. Jia, J. Zhang, W. Zhong, Y. Liang, K. Zhang, S. Dong, L. Ying, F. Liu, X. Wang, F. Huang and Y. Cao, *Nano Energy*, 2020, **72**, 104718.
6. P. Cheng and Y. Yang, *Acc. Chem. Res.*, 2020, **53**, 1218-1228.
7. X. Ma, J. Wang, J. Gao, Z. Hu, C. Xu, X. Zhang and F. Zhang, *Adv. Energy Mater.*, 2020, **10**, 2001404.
8. J. Yuan, Y. Zhang, L. Zhou, G. Zhang, H.-L. Yip, T.-K. Lau, X. Lu, C. Zhu, H. Peng, P. A. Johnson, M. Leclerc, Y. Cao, J. Ulanski, Y. Li and Y. Zou, *Joule*, 2019, **3**, 1140-1151.
9. J.-H. Lee, C.-H. Chen, P.-H. Lee, H.-Y. Lin, M.-k. Leung, T.-L. Chiu and C.-F. Lin, *J. Mater. Chem. C*, 2019, **7**, 5874-5888.
10. Y. Wada, H. Nakagawa, S. Matsumoto, Y. Wakisaka and H. Kaji, *Nat. Photon.*, 2020, **14**, 643-649.
11. X. Ban, A. Zhu, T. Zhang, Z. Tong, W. Jiang and Y. Sun, *Chem. Commun.*, 2017, **53**, 11834-11837.
12. D. Miguel, L. Álvarez de Cienfuegos, A. Martín-Lasanta, S. P. Morcillo, L. A. Zotti, E. Leary, M. Bürkle, Y. Asai, R. Jurado, D. J. Cárdenas, G. Rubio-Bollinger, N. Agraït, J. M. Cuerva

- and M. T. González, *J. Am. Chem. Soc.*, 2015, **137**, 13818-13826.
13. M. Moral, A. Garzón-Ruiz, M. Castro, J. Canales-Vázquez and J. C. Sancho-García, *J. Phys. Chem. C*, 2017, **121**, 28249-28261.
14. Z. B. Henson, K. Müllen and G. C. Bazan, *Nat. Chem.*, 2012, **4**, 699-704.
15. C. Sutton, C. Risko and J.-L. Brédas, *Chem. Mater.*, 2016, **28**, 3-16.
16. Z. Qiu, X. Xu, L. Yang, Y. Pei, M. Zhu, Q. Peng and Y. Liu, *Solar Energy*, 2018, **161**, 138-147.
17. S. Vegiraju, A. A. Amelanan Torimtubun, P.-S. Lin, H.-C. Tsai, W.-C. Lien, C.-S. Chen, G.-Y. He, C.-Y. Lin, D. Zheng, Y.-F. Huang, Y.-C. Wu, S.-L. Yau, G.-H. Lee, S.-H. Tung, C.-L. Wang, C.-L. Liu, M.-C. Chen and A. Facchetti, *ACS Appl. Mater. Interf.*, 2020, **12**, 25081-25091.
18. W. Zhang, Z. Mao, J. Huang, D. Gao and G. Yu, *Macromolecules*, 2016, **49**, 6401-6410.
19. H. Huang, L. Yang, A. Facchetti and T. J. Marks, *Chem. Rev.*, 2017, **117**, 10291-10318.
20. C. Fu, P. J. Beldon and D. F. Perepichka, *Chem. Mater.*, 2017, **29**, 2979-2987.
21. E. D. Głowacki, H. Coskun, M. A. Blood-Forsythe, U. Monkowius, L. Leonat, M. Grzybowski, D. Gryko, M. S. White, A. Aspuru-Guzik and N. S. Sariciftci, *Org. Electron.*, 2014, **15**, 3521-3528.
22. H. T. Black and D. F. Perepichka, *Angew. Chem. Int. Ed.*, 2014, **53**, 2138-2142.
23. Y. Wang, T. Hasegawa, H. Matsumoto and T. Michinobu, *J. Am. Chem. Soc.*, 2019, **141**, 3566-3575.
24. Á. J. Jiménez, M.-J. Lin, C. Burschka, J. Becker, V. Settels, B. Engels and F. Würthner, *Chem. Sci.*, 2014, **5**, 608-619.
25. M.-X. Zhang and G.-J. Zhao, *ChemSusChem*, 2012, **5**, 879-887.
26. Y. Zou, X. Ji, J. Cai, T. Yuan, D. J. Stanton, Y.-H. Lin, M. Naraghi and L. Fang, *Chem*, 2017, **2**, 139-152.
27. Y. Zou, T. Yuan, H. Yao, D. J. Frazier, D. J. Stanton, H.-J. Sue and L. Fang, *Org. Lett.*, 2015, **17**, 3146-3149.
28. B. P. Charron, M. U. Ocheje, M. Selivanova, A. D. Hendsbee, Y. Li and S. Rondeau-Gagné, *J. Mater. Chem. C*, 2018, **6**, 12070-12078.
29. M. U. Ocheje, B. P. Charron, Y.-H. Cheng, C.-H. Chuang, A. Soldera, Y.-C. Chiu and S. Rondeau-Gagné, *Macromolecules*, 2018, **51**, 1336-1344.
30. M. U. Ocheje, M. Selivanova, S. Zhang, T. H. Van Nguyen, B. P. Charron, C.-H. Chuang, Y.-H. Cheng, B. Billet, S. Noori, Y.-C. Chiu, X. Gu and S. Rondeau-Gagné, *Polym. Chem.*, 2018, **9**, 5531-5542.
31. L. Bai, P. Bose, Q. Gao, Y. Li, R. Ganguly and Y. Zhao, *J. Am. Chem. Soc.*, 2017, **139**, 436-441.
32. Z. Ding, H. Shang, S. Zhang, W. Han, B. Li and S. Jiang, *Cryst. Growth Des.*, 2020, **20**, 5203-5210.
33. W. Zhu, R. Zheng, Y. Zhen, Z. Yu, H. Dong, H. Fu, Q. Shi and W. Hu, *J. Am. Chem. Soc.*, 2015, **137**, 11038-11046.
34. E. Persch, O. Dumele and F. Diederich, *Angew. Chem. Int. Ed.*, 2015, **54**, 3290-3327.
35. C. Wang and Z. Li, *Mater. Chem. Front.*, 2017, **1**, 2174-2194.
36. A. N. Bootsma and S. E. Wheeler, *J. Chem. Inf. Model.*, 2019, **59**, 3413-3421.
37. A. N. Bootsma and S. E. Wheeler, *J. Chem. Inf. Model.*, 2019, **59**, 149-158.
38. M. O. Sinnokrot and C. D. Sherrill, *J. Phys. Chem. A*, 2004, **108**, 10200-10207.
39. N. J. Hestand and F. C. Spano, *Chem. Rev.*, 2018, **118**, 7069-7163.
40. C. A. Hunter and J. K. M. Sanders, *J. Am. Chem. Soc.*, 1990, **112**, 5525-5534.
41. E. A. Meyer, R. K. Castellano and F. Diederich, *Angew. Chem. Int. Ed.*, 2003, **42**, 1210-1250.
42. L. M. Salonen, M. Ellermann and F. Diederich, *Angew. Chem. Int. Ed.*, 2011, **50**, 4808-4842.
43. A. Y. Sosorev, V. A. Trukhanov, D. R. Maslennikov, O. V. Borshchev, R. A. Polyakov, M. S. Skorotetcky, N. M. Surin, M. S. Kazantsev, D. I. Dominskiy, V. A. Tafeenko, S. A. Ponomarenko and D. Y. Paraschuk, *ACS Appl. Mater. Interf.*, 2020, **12**, 9507-9519.
44. M.-H. Yoon, A. Facchetti, C. E. Stern and T. J. Marks, *J. Am. Chem. Soc.*, 2006, **128**, 5792-5801.
45. A. Faurie, C. Mallet, M. Allain, W. G. Skene and P. Frère, *New. J. Chem.*, 2016, **40**, 6728-6734.
46. C. Mallet, M. Allain, P. Leriche and P. Frère, *CrystEngComm*, 2011, **13**, 5833-5840.
47. H. R. Yakir, L. J. W. Shimon and O. Gidron, *Helv. Chim. Acta*, 2019, **102**, e1900027.
48. X.-Y. Li, M. Liu, K.-F. Yue, Y.-P. Wu, T. He, N. Yan and Y.-Y. Wang, *CrystEngComm*, 2015, **17**, 8273-8281.
49. E. C. Constable, C. E. Housecroft, S. Vujovic, J. A. Zampese, A. Crochet and S. R. Batten, *CrystEngComm*, 2013, **15**, 10068-10078.
50. T. M. Fasina, J. C. Collings, D. P. Lydon, D. Albesa-Jove, A. S. Batsanov, J. A. K. Howard, P. Nguyen, M. Bruce, A. J. Scott, W. Clegg, S. W. Watt, C. Viney and T. B. Marder, *J. Mater. Chem.*, 2004, **14**, 2395-2404.
51. L.-J. Han, Y.-J. Kong, N. Sheng and X.-L. Jiang, *J. Fluor. Chem.*, 2014, **166**, 122-126.
52. A. Hori, S. Takatani, T. K. Miyamoto and M. Hasegawa, *CrystEngComm*, 2009, **11**, 567-569.
53. U. H. F. Bunz, K. Seehafer, M. Bender and M. Porz, *Chem. Soc. Rev.*, 2015, **44**, 4322-4336.
54. X. Zhao, M. R. Pinto, L. M. Hardison, J. Mwaura, J. Müller, H. Jiang, D. Witker, V. D. Kleiman, J. R. Reynolds and K. S. Schanze, *Macromolecules*, 2006, **39**, 6355-6366.
55. M. Levitus, K. Schmieder, H. Ricks, K. D. Shimizu, U. H. F. Bunz and M. A. Garcia-Garibay, *J. Am. Chem. Soc.*, 2001, **123**, 4259-4265.
56. J. Ahner, M. Micheel, M. Enke, S. Zechel, U. S. Schubert, B. Dietzek and M. D. Hager, *Macromol. Chem. Phys.*, 2017, **218**, 1700343.
57. J. Kim, *Pure Appl. Chem.*, 2002, **74**, 2031-2044.
58. F. Zeng, L.-L. Tang, X.-M. Chen and M.-H. Ding, *Tetrahedron*, 2018, **74**, 6917-6921.
59. W. J. Mullin, R. H. Pawle, S. A. Sharber, P. Müller and S. W. Thomas, *J. Mater. Chem. C*, 2019, **7**, 1198-1207.
60. R. H. Pawle, T. E. Haas, P. Müller and S. W. Thomas, *Chem. Sci.*, 2014, **5**, 4184-4188.
61. S. A. Sharber, R. N. Baral, F. Frausto, T. E. Haas, P. Müller and S. W. Thomas, *J. Am. Chem. Soc.*, 2017, **139**, 5164-5174.
62. S. A. Sharber and S. W. Thomas, *Chem. Mater.*, 2020, **32**, 5785-5801.
63. W. J. Mullin, H. Qin, T. Mani, P. Müller, M. J. Panzer and S. W. Thomas, *Chem. Commun.*, 2020, **56**, 6854-6857.

64. G. J. Gabriel and B. L. Iverson, *J. Am. Chem. Soc.*, 2002, **124**, 15174-15175.
65. M. Hardouin-Lerouge, P. Hudhomme and M. Sallé, *Chem. Soc. Rev.*, 2011, **40**, 30-43.
66. S. K. Singh and A. Das, *Phys. Chem. Chem. Phys.*, 2015, **17**, 9596-9612.
67. B. Jeziorski, R. Moszynski and K. Szalewicz, *Chem. Rev.*, 1994, **94**, 1887-1930.
68. E. Papajak and D. G. Truhlar, *J. Chem. Theory Comput.*, 2011, **7**, 10-18.
69. K. Szalewicz, *Wiley Interdiscip. Rev: Compt. Mol. Sci.*, 2012, **2**, 254-272.
70. E. G. Hohenstein and C. D. Sherrill, *J. Chem. Phys.*, 2010, **133**, 014101.
71. E. G. Hohenstein and C. D. Sherrill, *J. Chem. Phys.*, 2010, **132**, 184111.
72. J.-D. Chai and M. Head-Gordon, *Phys. Chem. Chem. Phys.*, 2008, **10**, 6615-6620.
73. F. Weigend and R. Ahlrichs, *Phys. Chem. Chem. Phys.*, 2005, **7**, 3297-3305.
74. C. Adamo and V. Barone, *J. Chem. Phys.*, 1999, **110**, 6158-6170.
75. J. P. Perdew, M. Ernzerhof and K. Burke, *J. Chem. Phys.*, 1996, **105**, 9982-9985.
76. A. N. Bootsma, A. C. Doney and S. E. Wheeler, *J. Am. Chem. Soc.*, 2019, **141**, 11027-11035.
77. A. N. Bootsma and S. E. Wheeler, *ChemMedChem*, 2018, **13**, 835-841.
78. E. F. Pettersen, T. D. Goddard, C. C. Huang, E. C. Meng, G. S. Couch, T. I. Croll, J. H. Morris and T. E. Ferrin, *Protein Sci.*, 2021, **30**, 70-82.
79. A. J. Schaefer, V. M. Ingman and S. E. Wheeler, *J. Comput. Chem.*, 2021, **42**, 1750-1754.
80. V. M. Ingman, A. J. Schaefer, L. R. Andreola and S. E. Wheeler, *Wiley Interdiscip. Rev. Comput. Mol. Sci.*, 2021, **11**, e1510.

## TOC Image

